Journal of
Composites Science

MDPI

Article

Effect of Paraffin Microcapsule and Carbon Nanotube Content on the Thermal Behavior of Thermoplastic Polyurethane Nanocomposites with Thermal Energy Storage Capability

Daniele Rigotti *, Andrea Dorigato and Alessandro Pegoretti

Department of Industrial Engineering, University of Trento, Via Sommarive 9, and INSTM Research Unit, 38123 Trento, Italy; andrea.dorigato@unitn.it (A.D.); alessandro.pegoretti@unitn.it (A.P.)
* Correspondence: daniele.rigotti-1@unitn.it

Abstract

The development of multifunctional polymer composites capable of both heat conduction and latent heat storage is of great interest for advanced thermal management applications. In this work, thermoplastic polyurethane (TPU) nanocomposites containing microencapsulated paraffin-based phase change materials (PCMs) and multi-walled carbon nanotubes (MWCNTs) were systematically investigated. The microstructure, thermal stability, specific heat capacity, thermal diffusivity and conductivity of these composites were analyzed as a function of the PCM and MWCNTs content. SEM observations revealed the homogeneous dispersion of PCM microcapsules and the presence of localized MWCNT aggregates in PCM-rich domains. Thermal diffusivity measurements indicated a monotonic decrease with increasing temperature for all compositions, from 0.097 $mm^2 \cdot s^{-1}$ at 5 °C to 0.091 $mm^2 \cdot s^{-1}$ at 25 °C for neat TPU, and from 0.186 $mm^2 \cdot s^{-1}$ to 0.173 $mm^2 \cdot s^{-1}$ for TPU with 5 vol.% MWCNTs. Distinct non-linear behavior was observed around 25 °C, i.e., in correspondence to the paraffin melting, where the apparent diffusivity temporarily decreased due to latent heat absorption. The trend of the thermal conductivity (λ) was determined by the competing effects of PCM and MWCNTs: PCM addition reduced λ at 25 °C from 0.162 $W \cdot m^{-1} \cdot K^{-1}$ (neat TPU) to 0.128 $W \cdot m^{-1} \cdot K^{-1}$ at 30 vol.% PCM, whereas the incorporation of 5 vol.% of MWCNTs increased λ up to 0.309 $W \cdot m^{-1} \cdot K^{-1}$. In PCM-containing nanocomposites, MWCNT networks efficiently bridged the polymer–microcapsule interfaces, creating continuous conductive pathways that mitigated the insulating effect of the encapsulated paraffin and ensured stable heat transfer even across the solid–liquid transition. A one-dimensional transient heat-transfer model confirmed that increasing the matrix thermal conductivity accelerates the melting of the PCM, improving the dynamic thermal buffering capacity of these materials. Therefore, these results underlined the potential of TPU/MWCNT/PCM composites as versatile materials for applications requiring both rapid heat dissipation and effective thermal management.

Keywords: thermoplastic polyurethane; multi walled carbon nanotubes; phase change materials; thermal conductivity; thermal energy storage; thermal management

Academic Editor: Fubin Luo

Received: 25 November 2025
Revised: 9 December 2025
Accepted: 23 December 2025
Published: 1 January 2026

1. Introduction

Effective thermal management is a critical requirement in sectors such as aerospace, automotive and electronics, where maintaining components within optimal temperature ranges enhances their performance, reliability, and safety [1]. In applications ranging

from aircraft avionics to electric vehicle battery packs, preventing overheating is essential to avoid system failure, reduced lifespan, and potentially catastrophic events such as thermal runaway [2]. As devices become more compact and power-dense, the demand for advanced thermal management solutions continues to grow, driving research into innovative materials with superior heat storage and dissipation capabilities [3]. Phase change materials (PCMs) are widely recognized for their ability to store and release thermal energy during phase transitions, typically melting and solidification [4]. In particular, solid–liquid organic PCMs are especially attractive due to their high latent heat density and minimal volume change during phase transitions, making them suitable for building temperature regulation [5], intelligent textiles [6], and thermal management of batteries [7]. Among organic PCMs, paraffin waxes are the most widely investigated, because of their high thermal storage potential (up to 220 J/g), versatile phase transition temperature range (from −20 up to 110 °C) and relatively limited cost [8–10]. However, their widespread use is limited by the leakage of the PCM at the molten state and their inherently low thermal conductivity (and diffusivity), which considerably slows heat charging and discharging rates [11]. Encapsulation techniques, particularly microencapsulation with polymeric shells, address the leakage issue while enhancing handling and integration into composites [12,13]. Moreover, encapsulation increases surface area, improving heat transfer efficiency and enabling form-stable PCM composites with long-term stability [14].

Polymers, particularly thermoplastic matrices, are frequently employed to embed PCMs due to their flexibility, processability, and structural integrity [15,16]. Materials such as polyethylene (PE), polymethylmethacrylate (PMMA), and thermoplastic polyurethane (TPU) can effectively host microencapsulated PCMs [17,18], enabling the development of flexible, shape-stable composites suitable for textiles, building materials, and thermal interface layers [19]. However, most polymers exhibit very low thermal conductivity (0.1–0.5 W m^{-1} K^{-1}), due to weak inter-chain interactions, and high phonon scattering [20,21], this limits their efficiency in rapid thermal regulation applications. A common strategy to overcome this limitation is the incorporation of thermally conductive fillers into the polymer matrix. Carbon-based nanomaterials, such as carbon nanotubes (CNTs), graphene nanoplatelets, and carbon fibers, are particularly effective due to their high intrinsic thermal conductivity (up to several thousand W m^{-1} K^{-1}) [22] and ability to form conductive networks [20]. CNTs, in particular, offer high aspect ratios and one-dimensional conductive pathways that facilitate efficient phonon transport [20]. Even at low nanofiller loadings, they can significantly enhance polymer thermal conductivity, especially when well-dispersed and aligned within the hosting matrix [23]. Nevertheless, challenges remain in minimizing interfacial thermal resistance and avoiding filler agglomeration, which can reduce both thermal and mechanical performance of the resulting composites [24]. Surface functionalization and the introduction of hybrid fillers have been shown to mitigate these issues and improve filler–matrix compatibility [11]. PCM-filled flexible composites have gained attention in sports and outdoor performance gear due to their ability to dynamically regulate body temperature [25]. By absorbing excess heat during intense physical activity and releasing it when the body cools, PCM-enhanced textiles can maintain thermal comfort and reduce the risk of thermal stress [6]. Examples include gloves for ice climbing and cycling, activewear for endurance sports, and protective gear for extreme environments, where thermal stability directly affects performance and safety [26]. The integration of microencapsulated PCMs into fabrics preserves flexibility and mechanical integrity while providing dynamic thermal insulation, thus opening opportunities for high-performance sportswear with embedded thermal management capabilities [27]. In polymer composites containing PCMs, the addition of CNTs not only enhances thermal conductivity but can also influence mechanical properties [28]. While CNT introduction often increases stiffness,

the rigid shell of PCM microcapsules may reduce ductility [16], requiring careful formulation to balance thermal and mechanical performance. Optimized CNT/PCM/polymer systems have demonstrated stable latent heat storage capacity over repeated thermal cycles, high shape stability, and improved heat transfer rates [29], making them promising for advanced thermal management applications in wearable systems, battery enclosures, and smart building materials [30].

Despite the recognized relevance of flexible polymeric nanocomposite systems for thermal energy storage (TES) and their promising potential in various technological domains, a systematic understanding and modeling of their thermal properties have not yet been presented in the literature. Therefore, this study systematically investigated the thermal behavior of TPU-based nanocomposites incorporating microencapsulated PCMs and multi-walled carbon nanotubes (MWCNTs), focusing on the effect of CNT and PCM loading on the resulting thermal degradation resistance, thermal diffusivity and heat storage capacity. By systematically varying the MWCNT and PCM content, the synergistic effect of these fillers on heat transfer efficiency of the resulting TPU based formulations has been elucidated.

2. Materials and Methods

2.1. Materials

Thermoplastic polyurethane (TPU) Desmopan® 6064A (density 1.09 g cm^{-3}, melting temperature 200–220 °C) was supplied in form of granules by Covestro AG (Leverkusen, Germany). Microencapsulated phase change material (PCM) MPCM28D (hereafter M28D) was provided by Microtek Laboratories Inc. (Dayton, OH, USA) as a white powder. In M28D, a paraffin wax (PCM core) is encapsulated within a melamine–formaldehyde polymeric shell. The microcapsules exhibit a density of 0.95 g cm−3, a melting temperature (T_m) of 28 ± 2 °C, a mean diameter of 15–30 µm, and a melting enthalpy of 185 J g^{-1}, as specified by the manufacturer. Multi-walled carbon nanotubes (MWCNTs) NC7000™ were supplied by Nanocyl S.A. (Sambreville, Belgium): this nanofiller has an average length of 1.5 µm, an outer diameter of 9.5 nm, a specific surface area of 250–300 m^2 g^{-1}, and a density of 2.15 g cm^{-3}. All materials were dried under vacuum at 60 °C for 12 h prior to processing to remove residual moisture.

2.2. Sample Preparation

TPU granules were inserted in a Thermo Haake Rheomix 600 internal mixer (Thermo Fisher Scientific, Karlsruhe, Germany), equipped with counter-rotating rotors and operating at 200 °C and 60 rpm. After 2 min of mixing, MWCNTs were incorporated into the molten TPU; after an additional minute, M28D microcapsules were also added. The compound was then mixed for further 5 min. For samples without MWCNTs and/or PCM, the same total compounding time was utilized, to ensure the consistency of the processing conditions. The resulting compounds were then compression-molded using a Carver hot plate press at 180 °C for 10 min under a pressure of 1 MPa. In this way, square samples with a width of 120 mm and a mean thickness of 2 mm were prepared. For each CNT loading level (1, 3, and 5 vol.%), different amounts of paraffin (10, 20, and 30 phr) were incorporated (see Table 1). Sample codes indicate the matrix type and the relative content of MWCNTs and PCM. For example, TPU_5MWCNT_30M28D denotes a composition containing 5 vol.% MWCNTs and 30 phr of M28D.

Table 1. Composition of the prepared TPU/MWCNT/PCM nanocomposites.

Code	TPU Content (vol.%)	MWCNT Content (vol.%)	PCM Content (phr)
TPU	100	0	0
TPU_10 M28D	100	0	10
TPU_20 M28D	100	0	20
TPU_30 M28D	100	0	30
TPU_1MWCNT	99	1	0
TPU_1MWCNT_10M28D	99	1	10
TPU_1MWCNT_20M28D	99	1	20
TPU_1MWCNT_30M28D	99	1	30
TPU_3MWCNT	97	3	0
TPU_3MWCNT_10M28D	97	3	10
TPU_3MWCNT_20M28D	97	3	20
TPU_3MWCNT_30M28D	97	3	30
TPU_5MWCNT	95	5	0
TPU_5MWCNT_10M28D	95	5	10
TPU_5MWCNT_20M28D	95	5	20
TPU_5MWCNT_30M28D	95	5	30

2.3. Experimental Techniques

The density of neat TPU, MWCNTs and PCM was determined at 23 °C by helium pycnometry using a Micromeritics® Accupyc 1330 device (Micromeritics, Norcross, GA, USA) equipped with a 1 cm^3 chamber. 30 measurements were performed for each material. The apparent density values of the prepared nanocomposites, required for thermal conductivity calculations, were determined via the geometrical method by weighing samples of known dimension using a balance (accuracy ± 0.001 g) at 23 °C.

The morphology of the nanocomposites was investigated by field-emission scanning electron microscopy (FESEM) using a Carl Zeiss Supra 40 (Carl Zeiss AG, Oberkochen, Germany). Samples were fractured in liquid nitrogen, and the fractured surfaces were observed at an accelerating voltage of 2.5 kV. Prior to observation, all specimens were coated with a thin conductive Pt/Pd layer to prevent charging and enhance image resolution.

Thermal degradation behavior was assessed using a Q5000 IR thermogravimetric analyzer (TA Instruments, New Castle, DE, USA). Samples with a mass of about 10 mg were tested under a N_2 flow of 10 mL min^{-1} from 30 °C to 700 °C at a heating rate of 10 °C min^{-1}. The temperatures corresponding to 2% and 10% mass loss (T_2%, T_{10}%) and the residual mass at 700 °C (m_{700}) were determined. The maximum degradation rate temperature (T_{max}) was obtained from the derivative thermogravimetric (DTG) curves, which were further deconvoluted to identify the degradation peak of the different constituents.

The most important thermal transitions of the prepared materials were analyzed using a Mettler DSC 30 calorimeter (Mettler Toledo, Columbus, OH, USA), operating under a nitrogen flow of 100 mL min^{-1}. Samples with a mass of about ~10 mg were subjected to a heating–cooling cycle from −50 °C to 100 °C at a rate of 10 °C min^{-1}.

Thermal diffusivity measurements were carried out using a Netzsch LFA 467 HyperFlash (Netzsch, Selb, Germany) over a temperature range from –50 °C up to 50 °C, under an N_2 atmosphere of 250 mL min^{-1}. Prior to testing, specimens were coated with colloidal carbon to ensure complete absorption of the incident light pulse. The following testing parameters were adopted: voltage of 200 V, pulse width of 600 μs, and detection area diameter of 3.7 mm. Each sample was tested in quintuplicate to ensure reproducibility. Measurements between 5 °C and 50 °C were performed using a Venturi-effect cooling system with compressed air, while tests at lower temperature by employing liquid nitrogen. Measurements below 0 °C were necessary to properly fit the diffusivity data as a function of

temperature, as this approach minimized the influence of the latent heat in correspondence of the PCM melting temperature interval.

The specific heat capacity (c_p) of neat TPU, PCM, and MWCNTs was determined using a TA Instruments 2920 MDSC (TA Instruments, New Castle, DE, USA) according to ASTM E2716 standard [31], operating under a N_2 flow of 10 mL min^{-1} and in a temperature range from −20 °C to 70 °C. A synthetic sapphire disk was used as the reference material for c_p calibration. Calibration of both temperature and heat flow signals was performed in accordance with ASTM E967 and ASTM E968, respectively, and the specific heat capacity calibration constant K_{c_p} was determined at the midpoint of the temperature range of interest. A heating rate of 3 °C min^{-1}, with a modulated temperature amplitude of 1 °C and a frequency of 100 s, was applied. For neat PCM, additional modulated DSC tests were carried out at heating rate values ranging from 0.1 °C min^{-1} to 10 °C min^{-1}, to better characterize the apparent c_p behavior during the melting transition. This approach allowed distinguishing the reversible heat capacity from the enthalpic contribution associated with latent heat, as well as assessing the kinetic effects related to the rate-dependent melting of paraffin. The c_p of the nanocomposites was subsequently estimated using the rule of mixtures based on the weight fractions of the individual constituents [32]. Data in the range 5–50 °C were fitted to a linear model for subsequent processing. The c_p values were calculated as reported in Equation (1):

$$c_p = \frac{q}{m \cdot \Delta T} \tag{1}$$

where q is the measured heat flow (J), m the sample mass, and ΔT the temperature change.

The LFA method enabled the determination of the thermal conductivity (λ), determined according to Equation (2):

$$\lambda = \alpha \cdot c_p \cdot \rho \tag{2}$$

where α is the thermal diffusivity, c_p is the specific heat capacity and ρ is the density.

The transient heat transfer across the composite patch was modeled in Python 3.11.11 by numerically solving the one-dimensional heat conduction equation using an explicit finite-difference scheme. This approach allowed the temperature field and the phase change dynamics of the PCM to be resolved as a function of time and position, while ensuring numerical stability through the Courant–Friedrichs–Lewy (CFL) condition. The transient heat transfer across the composite patch was modeled by solving a one-dimensional heat conduction equation (Equation (3)):

$$\frac{\partial T}{\partial t} = \alpha \frac{\partial^2 T}{\partial x^2} \tag{3}$$

where $\alpha = \frac{k}{\rho c_p}$ is the thermal diffusivity. The domain was a flat slab with an isothermal boundary condition at the hot interface (50 °C) and an adiabatic condition at the opposite side, simulating the situation of a cooling patch attached to a warm surface while exposed to ambient air [33]. The composite was treated as an effective homogeneous medium, with its overall thermal properties (λ, ρ, c_p) computed by the rule of mixtures according to the PCM volume fraction.

The melting of the paraffin was modeled using the enthalpy method (Equation (4)), in which the latent heat dH_m is incorporated as an additional contribution to c_p over a narrow temperature interval ΔT centered at the melting temperature T_m:

$$c_{p,app} = c_p + \frac{dH_m}{\Delta T} \tag{4}$$

This temperature range ($T_m - \Delta T/2$, $T_m + \Delta T/2$) is called mushy zone [34], where solid and liquid phases coexist, and the PCM fraction gradually passes from solid ($f_L = 0$) to liquid ($f_L = 1$). In this zone, the heat input is partially stored as latent heat, slowing down the local temperature rise. The numerical scheme adopted was an explicit FTCS (Forward Time–Centered Space) finite difference method, with the CFL stability condition [35] satisfied (Equation (5)):

$$r = \frac{\alpha \Delta t}{\Delta x^2} \leq 0.5 \quad (5)$$

where r parameter, often referred to as the Fourier number for heat conduction, represents the ratio between the numerical time step and the characteristic diffusion time across a spatial cell ($\Delta x^2/\alpha$). Physically, it measures how far heat can diffuse within a single time increment compared to the grid spacing.

3. Results and Discussion

The densities of the individual constituents, i.e., TPU, microencapsulated PCM, and MWCNTs were determined by helium pycnometry at 23 °C, yielding values of 1.121 ± 0.005 g cm^{-3}, 0.956 ± 0.003 g cm^{-3}, and 2.150 ± 0.033 g cm^{-3}, respectively. These values were used as input parameters to calculate the theoretical density of the composites according to the rule of mixtures, based on the volume fractions of each component. The apparent geometrical density of the prepared nanocomposites was determined by measuring the mass and the volume of the prepared specimens. The results, summarized in Table 2, include the corresponding void content, expressed as the relative deviation between theoretical and measured densities.

Table 2. Geometrical and theoretical density of the prepared nanocomposites.

Code	Geometrical Density (g cm^{-3})	Theoretical Density (g cm^{-3})	Void Content (%)
TPU	1.105 ± 0.004	1.121 ± 0.005	1.43 ± 0.59
TPU_10 M28D	1.079 ± 0.005	1.099 ± 0.004	1.82 ± 0.59
TPU_20 M28D	1.041 ± 0.002	1.083 ± 0.004	3.91 ± 0.40
TPU_30 M28D	1.028 ± 0.006	1.070 ± 0.003	3.96 ± 0.61
TPU_1MWCNT	1.120 ± 0.002	1.126 ± 0.005	0.59 ± 0.46
TPU_1MWCNT_10M28D	1.074 ± 0.003	1.105 ± 0.004	2.81 ± 0.43
TPU_1MWCNT_20M28D	1.044 ± 0.005	1.088 ± 0.004	4.04 ± 0.55
TPU_1MWCNT_30M28D	1.013 ± 0.016	1.075 ± 0.003	5.80 ± 1.48
TPU_3MWCNT	1.114 ± 0.008	1.137 ± 0.005	2.05 ± 0.79
TPU_3MWCNT_10M28D	1.090 ± 0.003	1.115 ± 0.004	2.24 ± 0.44
TPU_3MWCNT_20M28D	1.060 ± 0.013	1.099 ± 0.004	3.58 ± 1.19
TPU_3MWCNT_30M28D	1.007 ± 0.007	1.085 ± 0.003	7.16 ± 0.73
TPU_5MWCNT	1.120 ± 0.011	1.148 ± 0.005	2.47 ± 1.05
TPU_5MWCNT_10M28D	1.092 ± 0.008	1.127 ± 0.004	3.11 ± 0.79
TPU_5MWCNT_20M28D	1.061 ± 0.005	1.110 ± 0.004	4.38 ± 0.58
TPU_5MWCNT_30M28D	1.051 ± 0.008	1.096 ± 0.003	4.14 ± 0.74

Neat TPU exhibits a void fraction of 1.43%, which falls within the experimental uncertainty and confirms the high compactness of the pristine matrix. In contrast, all filled systems display increasing void contents with filler loading, reaching approximately 4.1% in the formulation containing 30 vol.% PCM and 5 vol.% MWCNTs. This systematic increase suggests that the addition of microcapsules and nanotubes introduces structural heterogeneities that hinder complete compaction during melt processing. The formation of internal voids can be attributed to the combined effects of PCM microcapsules and CNTs. The fragile core–shell structure of the microcapsules may fracture under shear,

entrapping air pockets within the matrix [36]. Meanwhile, the inclusion of CNTs raises the melt viscosity of TPU, reducing the efficiency of air removal and limiting polymer flow into the interstitial regions [37,38].

Scanning electron microscopy (SEM) provided valuable insights into the morphological features and dispersion state of the fillers within the TPU matrix. Clear differences are observed between the neat polymer and the relative composites, reflecting the influence of both MWCNTs and PCM microcapsules on the microstructure. Neat TPU (Figure 1a) reveals a compact and homogeneous fracture surface, typical of an unfilled thermoplastic matrix. The absence of voids or cracks confirms the intrinsic continuity of the polymer phase When MWCNTs are introduced, as TPU_5MWCNT sample shown in Figure 1c, the surface remains relatively smooth, but the presence of micrometer-scale roughness and small irregularities become evident. These features can be ascribed to the nanotubes embedded within the TPU, which modify the fracture surface and create slight heterogeneities at the microscale. This morphology suggests that MWCNTs are well incorporated in the matrix, highlighting their ability to reinforce the polymer without significantly disrupting its continuity. A very different scenario is observed when PCM microcapsules are incorporated, as in TPU_30M28D sample shown in Figure 1b. The fracture surface displays a dense distribution of spherical voids corresponding to broken microcapsules, with variable size but generally well embedded within the matrix. Their morphology indicates that the encapsulated PCM was effectively dispersed during processing, avoiding large-scale segregation and maintaining a relatively uniform distribution within the polymer phase. The microcapsules appear well integrated, with no significant detachment from the matrix, suggesting good interfacial adhesion. The combined effect of MWCNTs and PCM microcapsules, exemplified by TPU_5MWCNT_30M28D sample shown in Figure 1d, results in a more complex morphology. The microcapsules remain clearly visible and well distributed throughout the matrix, but the nanotubes, now confined in the interstitial regions between capsules, show a tendency to form localized aggregates. This aggregation is not evident in the CNT-only filled composites, implying that the presence of microcapsules negatively affects the dispersion of MWCNTs within the TPU. The coexistence of two distinct fillers therefore leads to a more heterogeneous structure, where MWCNTs interact with both the TPU and the PCM microcapsule shells. Such morphological features are expected to influence the thermal response of the system: while the microcapsules provide elevated latent heat storage capability, the aggregated MWCNTs may locally enhance thermal conductivity but at the expense of uniform dispersion. Overall, these observations highlight the delicate balance between filler dispersion and interfacial interactions in multiphasic TPU composites.

Thermogravimetric analysis (TGA) provides a quantitative assessment of mass loss as a function of temperature, allowing the evaluation of the thermal stability and decomposition behavior of the prepared materials. Figure 2a shows the TGA curves of neat TPU and the relative nanocomposites, while Figure 2b reports the corresponding derivative thermogravimetric (DTG) curves. The most relevant parameters, i.e., the temperatures associated with a mass loss of 2%, and 10% (T_2%, T_{10}%) and residual mass at 700 °C (m700), are summarized in Table 3. For all the formulations, the main degradation stage starts above 300 °C, but two additional degradation steps are evident. The first occurs above 100 °C and is more pronounced in samples containing PCM, with intensity proportional to the microcapsule content. This explains the lower T_2%, and T_{10}% values compared to neat TPU. Such behavior can be attributed to partial rupture of microcapsules during melt compounding and compression molding, causing paraffin leakage and its subsequent evaporation at relatively low temperatures. Another notable difference between neat TPU and the composites is the presence of residual mass in the latter (2–4%), due to the decom-

position products of the melamine–formaldehyde shell of PCM. DTG curves (Figure 2b) reveal two distinct degradation peaks between 300 and 500 °C for the materials loaded with PCM, confirming the positive contribution of the microcapsule shell to thermal stabilization. Regarding residual mass at 700 °C, Table 3 shows a general decrease with increasing PCM content, particularly at elevated CNT amounts. This trend suggests that, although the microcapsule shell contributes to char formation, the higher paraffin fraction leads to the evolution of a greater concentration of volatile products, lowering the final residue.

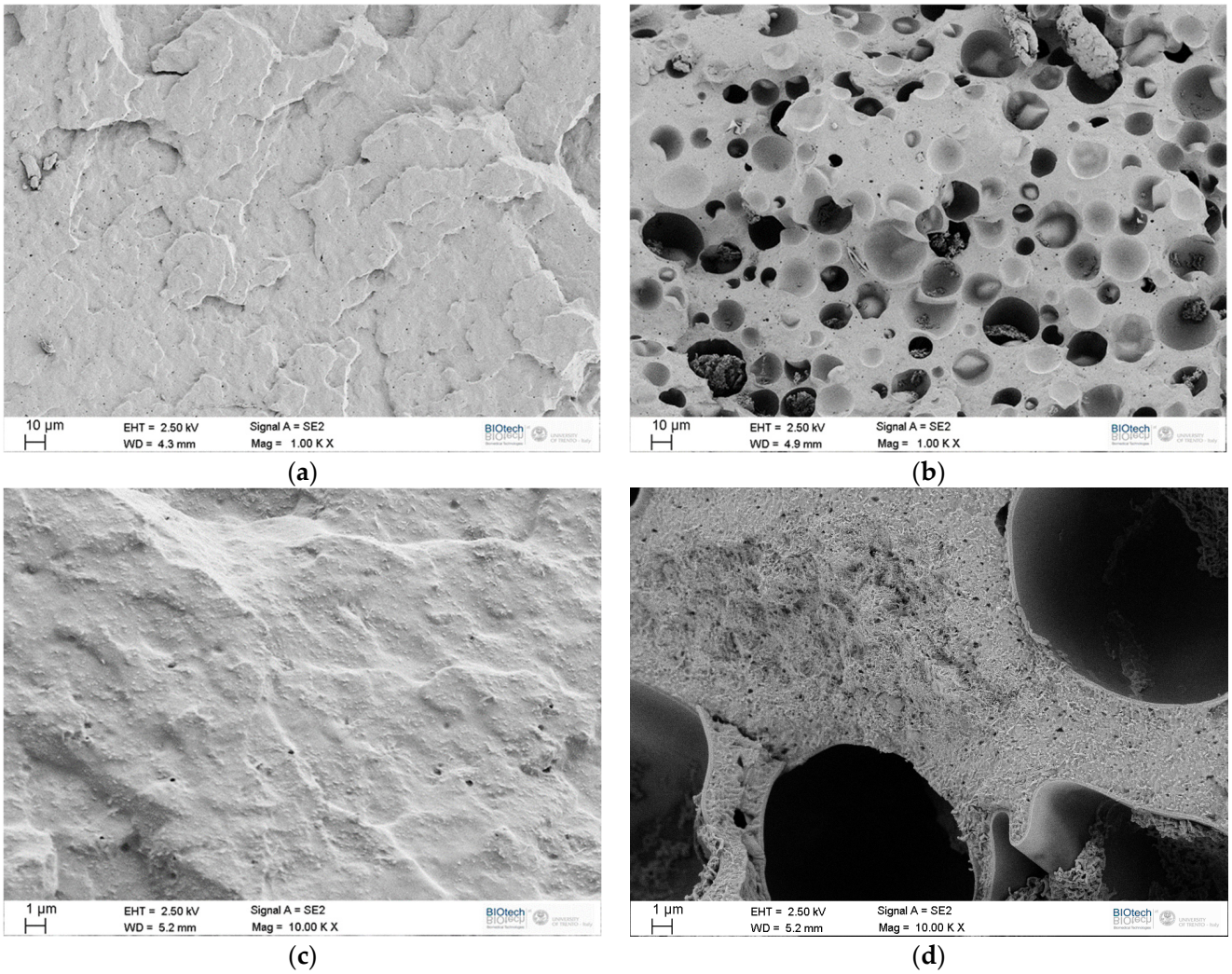

Figure 1. SEM micrographs of the fracture surfaces of (**a**) TPU, (**b**) TPU_30M28D, (**c**) TPU_5MWCNT, and (**d**) TPU_5MWCNT_30 M28D samples.

The TGA results indicate that PCM content is the dominant factor affecting both T_2% and T_{10}%, whereas the effect of CNT content is not statistically significant. The surface plot for T_2% (Figure 3a) shows a clear monotonic decrease in degradation onset temperature (T2%) with increasing PCM content, independent of MWCNT concentration. The highest T_2% values (~280 °C) occur at low PCM content, whereas the lowest values (~160 °C) are associated with the highest PCM loading, reflecting the early mass loss due to paraffin evaporation from damaged microcapsules. Similarly, the surface plot for T_{10}% (Figure 3b) displays the same overall trend, although the observed reduction is less steep. The highest T_{10}% values (>330 °C) are found in formulations with low PCM and high MWCNT content, while the lowest values (~305 °C) correspond to high PCM amounts.

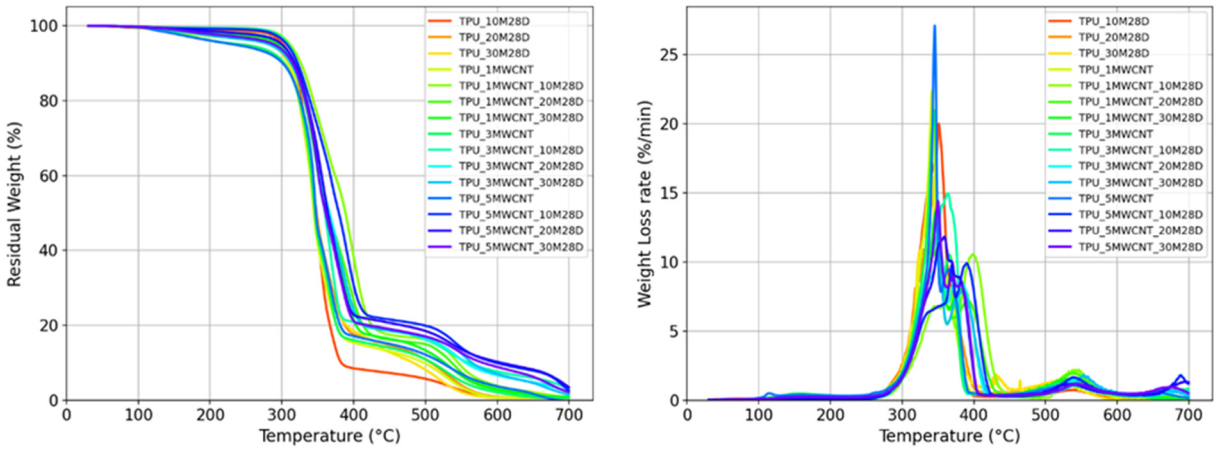

(**a**) (**b**)

Figure 2. (**a**) Thermogravimetric curves and (**b**) corresponding derivative thermogravimetric (DTG) curves of neat TPU and the relative nanocomposites.

Table 3. Results of TGA tests of neat TPU and the relative nanocomposites.

Sample	$T_{2\%}$ (°C)	$T_{10\%}$ (°C)	m_{700} (%)
TPU	278.0	316.6	0.6
TPU_10M28D	254.4	310.0	0.7
TPU_20 M28D	176.6	308.5	0.7
TPU_30 M28D	164.1	310.9	0.6
TPU_1MWCNT	293.0	326.5	0.9
TPU_1MWCNT_10M28D	217.8	316.1	0.6
TPU_1MWCNT_20M28D	194.0	316.1	0.8
TPU_1MWCNT_30M28D	153.9	303.4	0.6
TPU_3MWCNT	291.1	321.8	3.1
TPU_3MWCNT_10M28D	241.0	317.5	2.2
TPU_3MWCNT_20M28D	176.3	312.5	1.5
TPU_3MWCNT_30M28D	147.0	301.1	0.3
TPU_5MWCNT	285.8	322.0	2.7
TPU_5MWCNT_10M28D	238.4	318.2	3.5
TPU_5MWCNT_20M28D	189.8	315.1	2.1
TPU_5MWCNT_30M28D	159.3	302.1	2.8

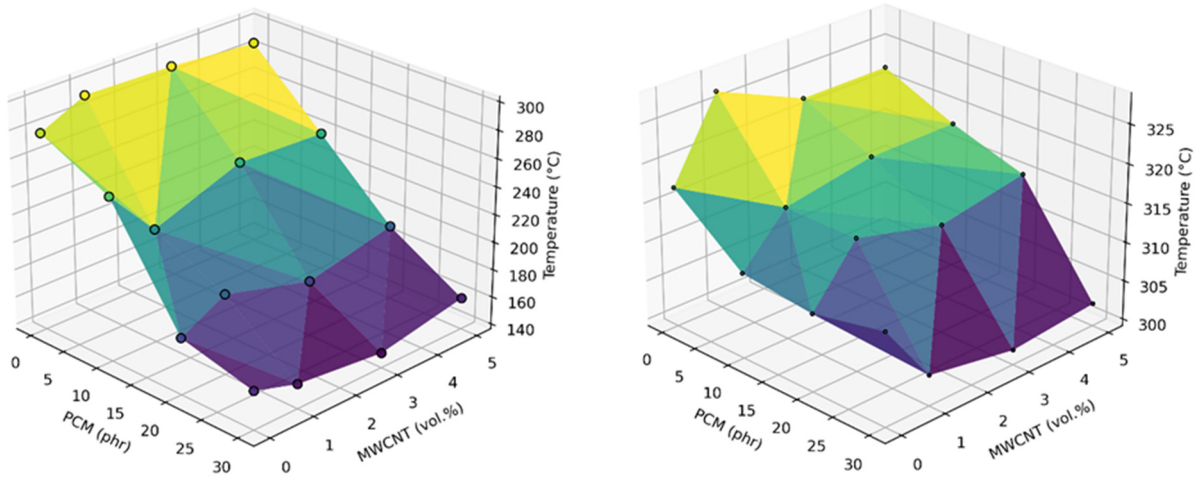

(**a**) (**b**)

Figure 3. (**a**) Surface plots showing the influence of PCM and MWCNT content on (**a**) temperature at 2% weight loss (T_2%), (**b**) temperature at 10% weight loss (T_{10}%), determined in TGA tests.

Deconvolution analysis applied to DTG curves (see Figure 4) shows that TPU undergoes two main degradation stages (Figure 4a), with the hard segments decomposing at ~340 °C and the soft segments at ~360 °C. This behavior is consistent with previously reported thermal decomposition pathways in segmented polyurethanes [39,40]. A minor high-temperature degradation step, appearing around 550 °C and visible only in the DTG trace, is likely related to C–C bond cleavage accompanied by advanced chain fragmentation, dehydrogenation, and gasification [41,42]. In PCM containing samples (Figure 4b,c), the deconvolution curves reveal a sharp, spike-like peak centered at ~345 °C, which can be attributed to the rupture of the melamine–formaldehyde shell and the rapid evaporation of the encapsulated paraffin [16]. In the case of TPU_5MWCNT nanocomposites (Figure 4c), a clear improvement in thermal stability is observed compared to neat TPU. The deconvolution analysis shows that the onset and maximum degradation stages are shifted toward higher temperatures, with the first DTG peak moving from 331 °C to 343 °C and the second from 347 °C to 367 °C. A similar upward shift is also visible for the high-temperature shoulder, which moves from ~526 °C in neat TPU to ~545 °C in TPU_5MWCNT. In addition, a third degradation event appears above 650 °C, which can be attributed to the progressive decomposition of carbonaceous residues. The overall stabilization effect induced by MWCNTs is commonly ascribed to the formation of a CNT-rich char and a tortuous diffusion pathway that effectively hinders the transport of volatile degradation products and oxygen, together with the enhanced heat dissipation associated with the high intrinsic thermal conductivity of the nanotubes [43–45].

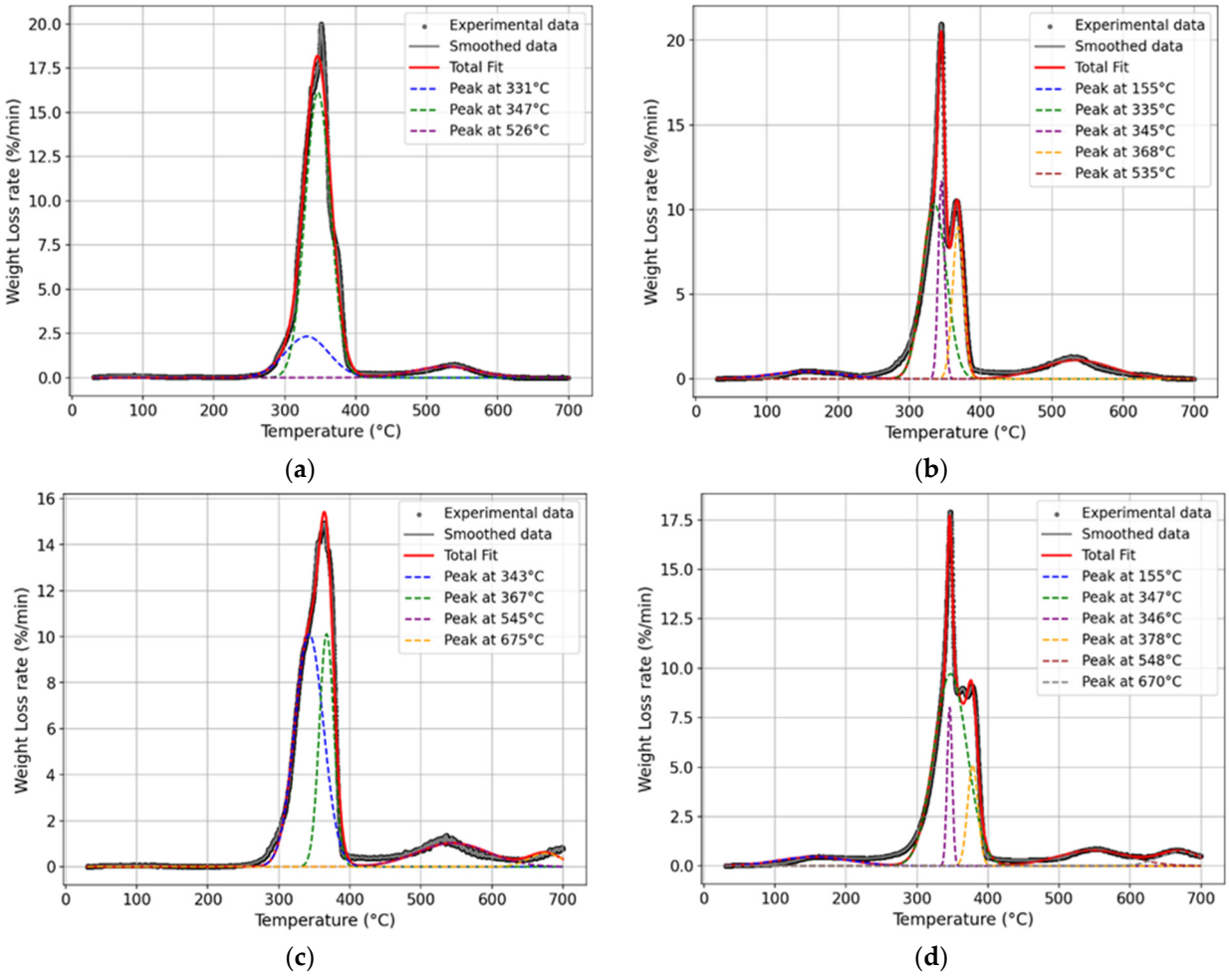

Figure 4. Deconvolution of DTG curves of (**a**) TPU, (**b**) TPU_1MWCNT_30M28D, (**c**) TPU_5MWCNT, and (**d**) TPU_5MWCNT_30M28D samples.

DSC analysis was performed to evaluate the thermal transitions associated with the melting and crystallization of the PCM phase in the prepared nanocomposites. Figure 5a shows DSC thermograms collected in the first heating scan, while Figure 5b the curves collected in the cooling stage. Table 4 summarizes the melting and crystallization behavior of the PCM-containing composites, including the transition enthalpies (ΔH_m and ΔH_c) and the corresponding peak temperatures derived from the heating and cooling scans, respectively. As expected, neat TPU and TPU/MWCNT composites without PCM exhibit no endothermic or exothermic peaks within the investigated temperature range. In contrast, all PCM-containing samples display well-defined melting and crystallization peaks, whose magnitude increases with the PCM content. The melting enthalpy rises from approximately 16 $J \cdot g^{-1}$ for TPU_10M28D to 52 $J \cdot g^{-1}$ for TPU_30M28D, while the corresponding crystallization enthalpy follows a similar trend, increasing from 17 $J \cdot g^{-1}$ to 51 $J \cdot g^{-1}$. The melting temperatures lie in the 27–31 °C range, while the crystallization peaks occur between 7 °C and 12 °C, consistent with the typical thermal behavior of paraffin-based PCMs. The observed temperature gap between melting and crystallization is attributed to the supercooling typically associated with the solidification of crystalline materials. Minor variations among samples, such as the slightly higher melting temperatures observed at greater PCM loadings, may arise from differences in local heat transfer within the matrix or in the thermal coupling between adjacent capsules. Notably, the inclusion of MWCNTs does not significantly alter either the melting or crystallization temperatures, nor the corresponding enthalpy values, suggesting that MWCNT addition does not interfere with the phase transition of the encapsulated PCM. Furthermore, the close agreement between the latent heat values measured during heating and cooling confirms the reproducibility of the transitions and the thermal stability of the microencapsulated PCM within the TPU matrix.

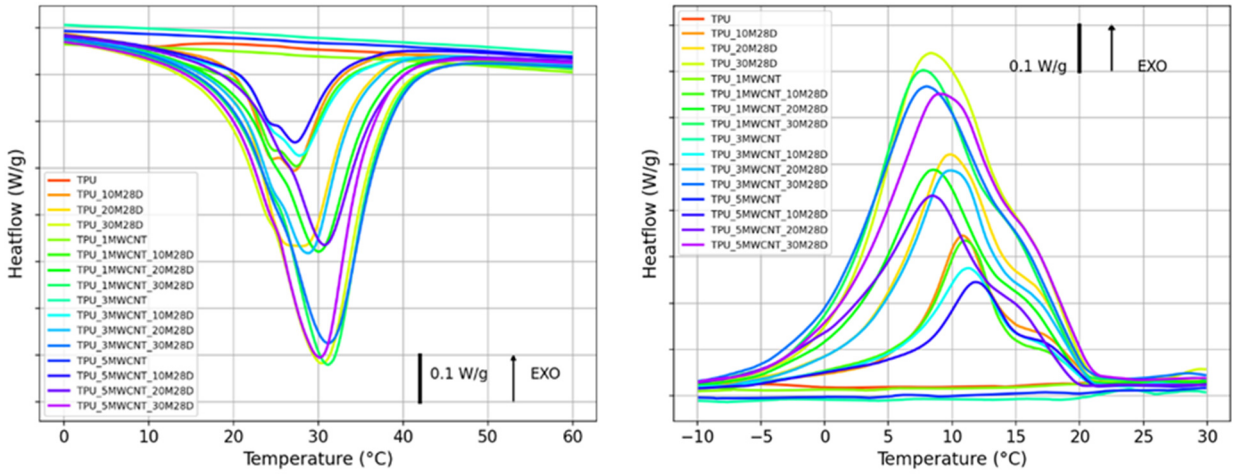

Figure 5. DSC thermograms of neat TPU and the relative nanocomposites in the region of melting/crystallization of PCM. (**a**) First heating scan, (**b**) cooling scan.

Figure 6 shows the relationship between the theoretical PCM weight fraction and the values experimentally determined from DSC measurements. The experimental data closely follows the expected trend (dotted line) at a theoretical PCM content of 10 phr, confirming that the measured enthalpy changes are consistent with the nominal PCM content, confirming the absence of a significant PCM loss during melt compounding and/or hot pressing. However, at higher PCM concentrations (20 phr and 30 phr), a progressive negative deviation from the theoretical line is observed. This discrepancy may be attributed to partial leakage or volatilization of PCM during processing, especially at elevated temperatures. The calculated latent heat values, once normalized to the effective PCM fraction, remain

comparable to those of neat paraffin microcapsules ($\Delta H_m \approx 217.4$ J g^{-1}), confirming that the phase-change capability of the encapsulated PCM is largely preserved after processing, despite the expected deviations associated with manufacturing-induced PCM leakage [16]. The behavior observed here is consistent with that of similar TPU/PCM systems prepared by our group using similar microencapsulated paraffin with a melting temperature of 6 °C (M6D). In that work, the melting and crystallization enthalpy of TPU/M6D composites scaled linearly with PCM content up to 60 wt%, with normalized latent heat values between 83% and 97% of the theoretical value of neat PCM. These results indicated that most of the encapsulated paraffin actively participated in the phase change process despite being embedded in the polymer matrix.

Table 4. Results from DSC tests regarding the thermal properties of PCM.

Sample	ΔH_m (J/g)	T_m (°C)	ΔH_c (J/g)	T_c (°C)
TPU	-	-	-	-
TPU_10M28D	16.0	27.2	17.4	10.8
TPU_20 M28D	31.2	28.0	33.1	9.8
TPU_30 M28D	52.6	30.5	50.7	8.3
TPU_1MWCNT	-	-	-	-
TPU_1MWCNT_10M28D	16.2	27.5	16.6	11.0
TPU_1MWCNT_20M28D	31.9	30.0	32.2	8.5
TPU_1MWCNT_30M28D	49.6	31.2	50.1	7.7
TPU_3MWCNT	-	-	-	-
TPU_3MWCNT_10M28D	14.4	27.7	16.2	11.3
TPU_3MWCNT_20M28D	31.3	28.8	32.1	9.8
TPU_3MWCNT_30M28D	51.1	31.2	48.9	8.0
TPU_5MWCNT	-	-	-	-
TPU_5MWCNT_10M28D	14.1	27.3	14.7	11.8
TPU_5MWCNT_20M28D	30.1	30.7	31.3	8.5
TPU_5MWCNT_30M28D	48.5	30.2	49.8	9.0
Neat PCM	217.4	28.3	206.2	10.2

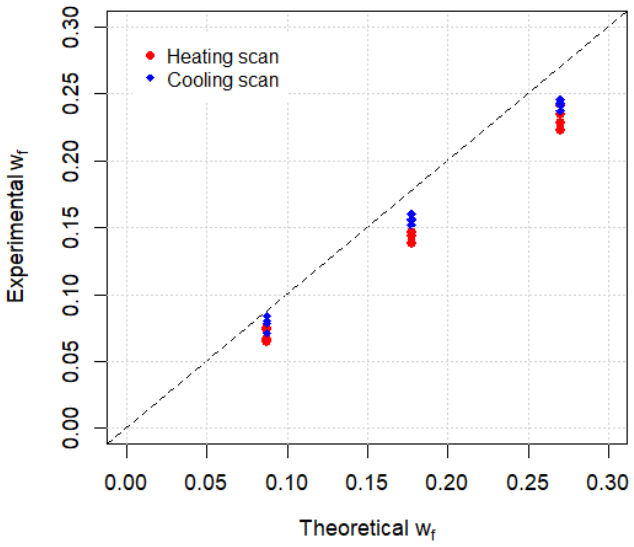

Figure 6. Experimental PCM weight fraction extrapolated from DSC results against theoretical PCM content, the dotted line indicates the expected value.

Thermal diffusivity measurements (see Figure 7a,d) reveal a clear dependence on both temperature and filler content. Neat TPU and TPU filled with MWCNTs exhibit a monotonic decrease in diffusivity with increasing temperature in the range 5–50 °C, with statistically significant negative slopes at all MWCNT concentrations ($p < 0.05$). This trend

is consistent with the typical behavior of polymeric systems, where increasing temperature enhances segmental motion of the molecular chains, leading to increased phonon scattering and, consequently, a reduction in thermal transport efficiency [46]. A similar temperature-dependent decrease in thermal diffusivity has been widely reported for amorphous and semi-crystalline polymers filled with carbon-based nanomaterials [47]. The incorporation of MWCNTs systematically enhances the diffusivity, with values nearly doubling between 0 and 5 vol.% CNT. For instance, at 5 °C diffusivity increases from 0.097 mm^2 s^{-1} °C in neat TPU to 0.186 mm^2 s^{-1} in TPU with 5 vol.% MWCNT at the same temperature. In samples containing microencapsulated PCM, diffusivity also decreases with temperature, but a marked nonlinearity can be observed in the 20–30 °C interval, coinciding with the paraffin melting transition. This apparent drop in diffusivity can be explained considering that, during the phase change, the heat supplied to the material is absorbed as latent heat rather than contributing to a temperature increase. As a result, the rate of temperature increase slows down, and the heat propagates more slowly through the material. This results in a reduction in apparent thermal diffusivity, since the underlying assumption of constant heat flow, implicit in the laser flash analysis, is no longer valid when part of the energy is consumed by the endothermic melting process of the paraffin. The extent of diffusivity reduction is scaled with PCM loading, with the relative decrease between 5 and 25 °C averaging −16.8%, −24.1% and −30.2% for 10, 20 and 30 vol.% PCM, respectively, compared to −3.5% for neat TPU. The minimum diffusivity occurs near 25 °C, consistent with DSC data, and this is mitigated by the presence of CNTs, which provide faster conductive pathways that distribute heat more uniformly within the matrix, thus reducing the apparent loss of diffusivity during melting.

To remove the latent heat effect and obtain more reliable diffusivity values across the melting interval, additional LFA tests were performed in the temperature range from −50 °C to −5 °C. These measurements were used exclusively to approximate the thermal diffusivity trend with a linear model and to extrapolate the expected values in the paraffin melting transition. However, data collected at subzero temperatures exhibited significant scatters, most likely due to the liquid nitrogen cooling system. The intense nitrogen flow may have introduced signal instabilities in the detector and promoted condensation on the sample surface, thereby compromising measurement accuracy. For this reason, the subzero diffusivity data are not discussed further in this work, as their purpose was limited to refining the interpolation of diffusivity values within the paraffin melting range.

These findings indicate the complementary contribution between MWCNTs and PCM: MWCNT not only enhances the thermal diffusivity of the composite but also partially compensates for the reduction in diffusivity caused by the paraffin phase transition, enabling both rapid heat transfer and transient thermal buffering. This dual effect highlights the potential of TPU/MWCNT/PCM blends for advanced thermal management applications, where fast thermal response and effective temperature regulation must be balanced.

The specific heat capacity of the constituents (TPU, MWCNTs, and PCM) was determined by modulated DSC according to ASTM E2716. The resulting c_p (T) curves are reported in Figure 8. Neat TPU (Figure 8a) exhibits a nearly linear increase in c_p with temperature, ranging from approximately 1.46 $J \cdot g^{-1} \cdot K^{-1}$ at 0 °C to 1.68 $J \cdot g^{-1} \cdot K^{-1}$ at 60 °C. The measured values and their linear trend with temperature for TPU are consistent with those reported in the literature [48]. The specific heat capacity of carbon nanotubes reported in the literature spans a relatively broad range depending on morphology and synthesis route, typically between 0.13 and 0.70 $J \cdot g^{-1} \cdot K^{-1}$ at room temperature [49]. For instance, values of 0.312 $J \cdot g^{-1} \cdot K^{-1}$ and 0.700 $J \cdot g^{-1} \cdot K^{-1}$ have been reported for MWCNTs prepared via chemical vapor deposition [50], while experiments on MWCNT films report a range of 0.133–0.496 $J \cdot g^{-1} \cdot K^{-1}$ [51]. More recent studies on densified and functionalized CNT

have shown even higher cp values, approaching 1 J·g^{-1}·K^{-1}, as a consequence of increased defect density and inter-tube interactions enhancing phonon scattering [52,53]. These findings are consistent with the results obtained in this work by modulated DSC, confirming the reliability of the experimental approach adopted in the present work (Figure 8b). For the PCM containing samples, a challenge arose due to the first-order phase transition (PCM melting) occurring near 28 °C. During melting, ΔT tends to zero while heat is absorbed, leading to an apparent divergence of c_p. To investigate this effect, additional tests at different heating rates (0.1, 1, 3, 5, and 10 °C min−1) were performed (Figure 8c). Increasing the heating rate broadens the apparent c_p peak and shifts it to higher temperatures, whereas low heating rates indicate that the onset of the phase transition in paraffin occurs slightly below 28 °C. This trend agrees with previous reports highlighting the strong dependence of the apparent c_p on the heating rate [54,55]. According to Fatahi et al. and Sun et al., higher heating rates lead to an artificial broadening and shift of the c_p peak due to thermal lag and sensor response limitations. Conversely, when the heating rate is reduced, the transition occurs closer to thermodynamic equilibrium temperature, leading to a smoother c_p curve. At the theoretical limit of a zero-heating rate, the reversible c_p signal would flatten, and the apparent c_p peak associated with latent heat would disappear, as the system evolves quasi-statically with no measurable temperature difference between the sample and the reference. Following established DSC/MDSC practice, the sensible heat capacity in the melting interval was reconstructed by linear interpolation between the linearly fitted sub- and supra-melting regions, effectively removing the latent contribution. Results are reported in Table 5 and the graphical construction is visible in Figure 8d. This workflow is consistent with ISO 11357-3:2018baseline constructions and ASTM E2716-19separation of reversing (sensible c_p) from non-reversing heat flow [56,57]. To refine this correction and ensure continuity across the melting interval, the specific heat capacity values were interpolated between the two fitted linear regions, corresponding, respectively, to the solid and liquid states of the paraffin. The temperature boundaries of the melting range were determined as the points where the experimental c_p deviated by more than 1% from the fitted lines on both sides of the transition. Between these two deviation points, c_p values were replaced by a linear segment connecting the end points of the pre- and post-transition fits. This interpolation provides a continuous, piecewise-linear c_p curve that preserves the physical behavior of the material while removing the distortion introduced by the latent heat. The resulting dataset allows reliable use of PCM heat capacity values in thermal conductivity calculations, ensuring that the computed thermal transport properties reflect only the sensible heat contribution rather than the transient energy storage associated with phase change.

Table 5. Specific heat capacity values at different temperatures of TPU, MWCNT and PCM constituents extrapolated via linear fitting of reversible c_p signal from MDSC.

Temperature (°C)	Specific Heat Capacity (J g^{-1} K^{-1})		
	TPU	MWCNT	M28D
5	1.482	0.929	1.607
10	1.500	0.946	1.649
15	1.518	0.963	1.691
20	1.536	0.981	1.734
25	1.554	0.998	1.776
30	1.572	1.015	1.818
35	1.590	1.033	1.861
40	1.607	1.050	1.903
45	1.625	1.067	1.945
50	1.643	1.085	1.965

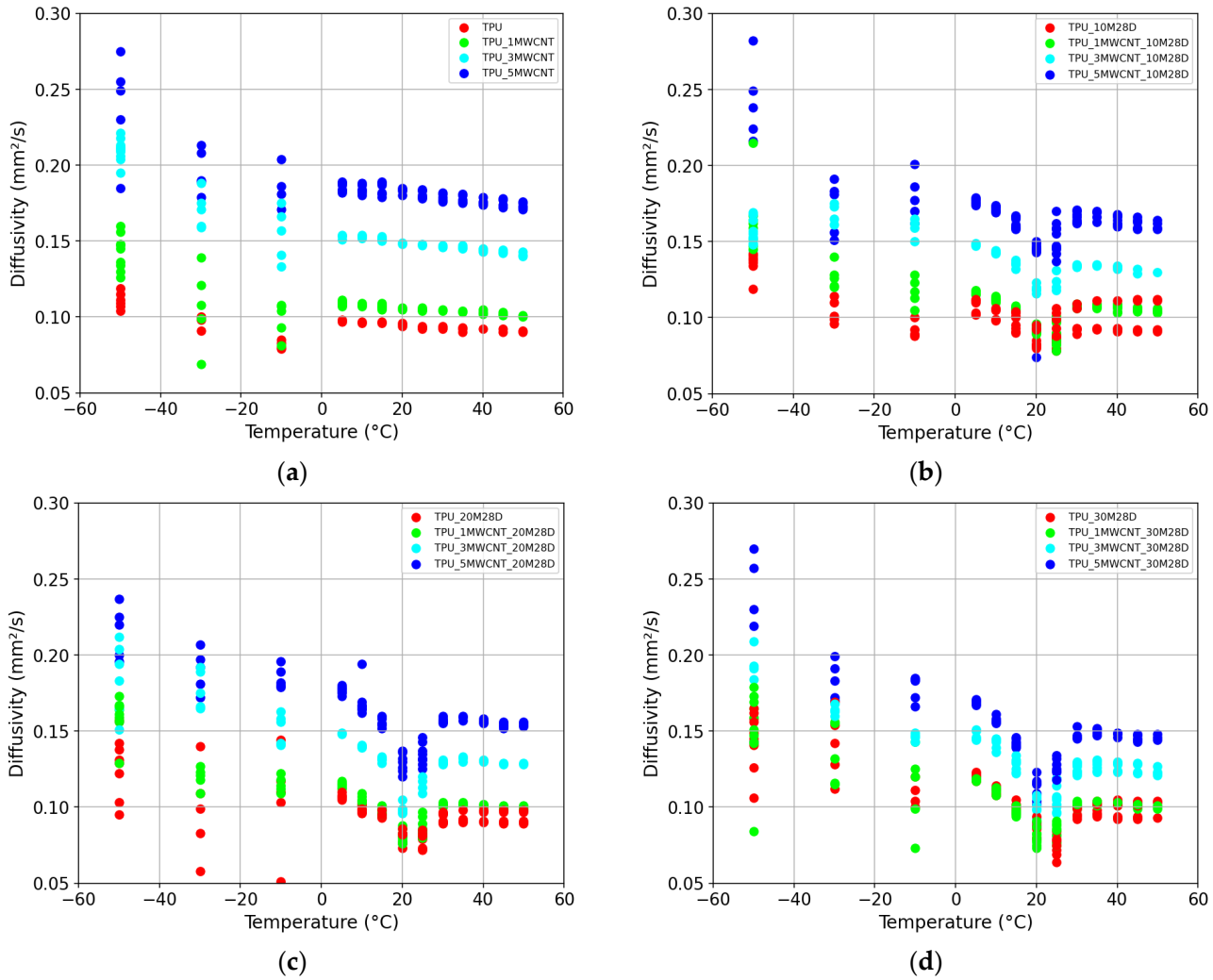

Figure 7. Thermal diffusivity of the prepared samples as a function of temperature: (**a**) neat TPU and CNT-filled systems without PCM, (**b**) composites with 10 vol.% PCM, (**c**) composites with 20 vol.% PCM, and (**d**) composites with 30 vol.% M28D.

The thermal conductivity values at different temperatures were calculated according to Equation (2), where the thermal diffusivity was obtained from LFA measurements, the specific heat capacity from MDSC analysis, and the geometrical density. The resulting conductivities are presented in Figure 9 as 3D plots, showing their dependence on composition below (Figure 9a) and above (Figure 9b) the PCM melting temperature, while the complete dataset for all samples and temperatures is summarized in Table 6. The results reveal a clear interplay between the insulating effect of the PCM and the conductive contribution of carbon nanotubes. Neat TPU exhibits the lowest conductivity across the entire temperature range, with values increasing slightly from 0.160 W m^{-1} K^{-1} at 5 °C to 0.166 W m^{-1} K^{-1} at 50 °C, reflecting the limited phonon transport typical of thermoplastic polymers.

The incorporation of paraffin microcapsules leads to a systematic reduction in thermal conductivity near the transition temperature, which becomes more pronounced with increasing PCM content. Conversely, the addition of MWCNTs significantly enhances the thermal conductivity. For instance, at 5 °C the thermal conductivity nearly doubles from 0.160 W m^{-1} K^{-1} in neat TPU to 0.302 W m^{-1} K^{-1} in the composite containing 5 vol.% MWCNTs. This improvement is attributed to the formation of a thermally conductive percolation network that facilitates phonon transfer across the polymer matrix. In systems combining both fillers, the competing effects of the insulating PCM and conduc-

tive CNTs are evident: while PCM addition decreases conductivity, the presence of CNTs effectively mitigates this reduction, maintaining relatively high values even at high microcapsule loadings. The influence of temperature further increases these trends, as illustrated in Figure 9. At 20 °C (Figure 9a), i.e., below the paraffin melting point, the competing effects of CNTs and M28D are clearly visible: microcapsules lower the conductivity, while CNTs strongly compensate and even dominate when present at higher concentrations. At 40 °C (Figure 9b), above the Tm of paraffin, the overall conductivity increases for all compositions compared to 20 °C. This rise reflects the end of the solid–liquid transition, after which the absorbed latent heat no longer contributes to an apparent loss in thermal conductivity. Around the transition temperature (~25 °C), however, a temporary decrease in apparent conductivity can be observed in PCM-containing samples. This drop originates from the energy absorbed by paraffin during melting, which shortly reduces the portion of heat conducted through the composite. Once the phase change is complete, conductivity values return to a stable regime, approaching those predicted by the rule of mixtures. CNT networks are crucial in this context, as they maintain continuous conductive pathways across both solid and liquid states of PCM, mitigating the loss of transport efficiency and ensuring more stable thermal performance across the operational range.

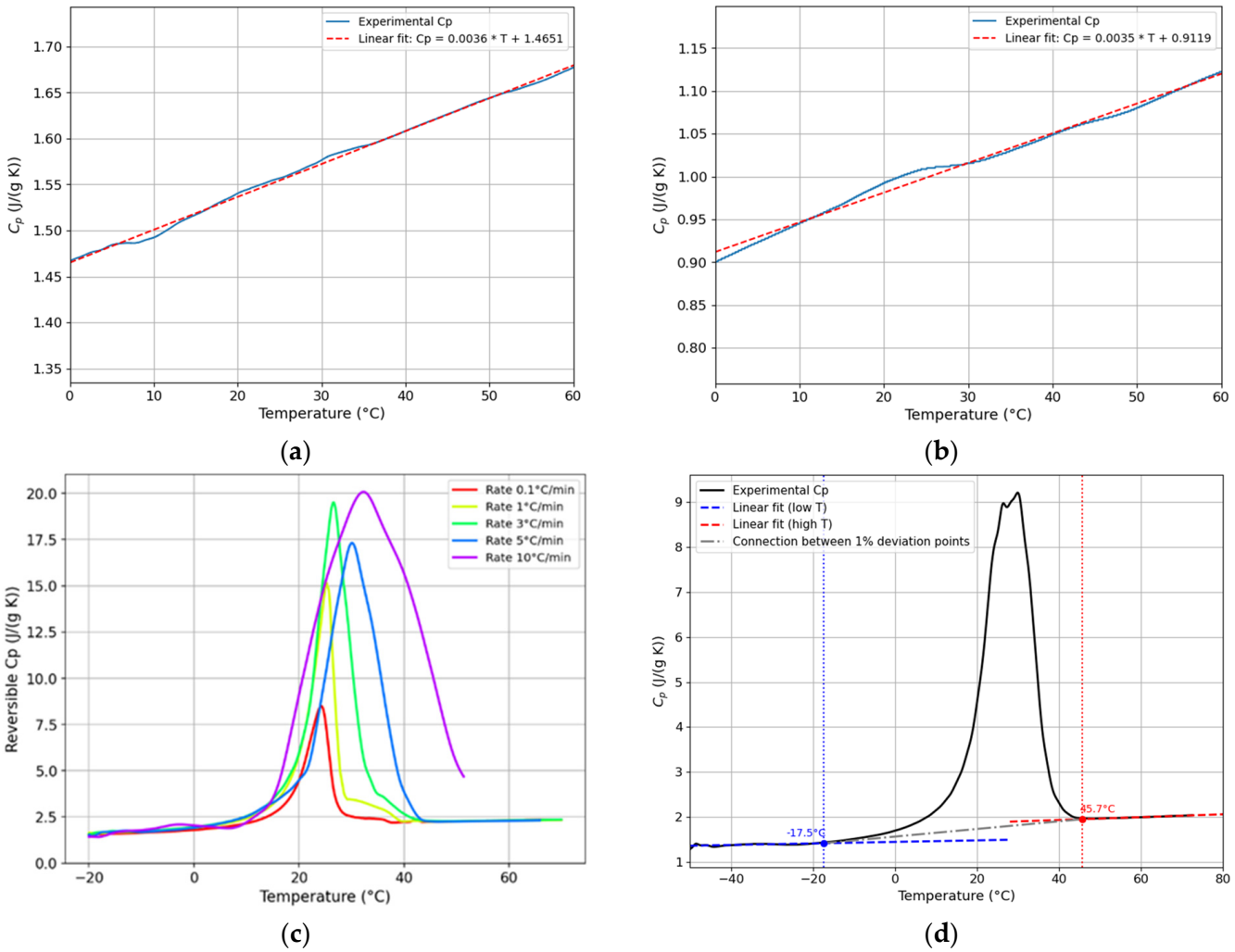

Figure 8. Determination of specific heat capacity from MDSC data. Linear fitting of the c_p for (**a**) neat TPU and (**b**) MWCNTs. (**c**) Effect of different heating rates on the apparent c_p of PCM in the temperature interval across its melting point; (**d**) extrapolation of the c_p of PCM in the proximity of the melting peak, excluding the contribution of the phase transition.

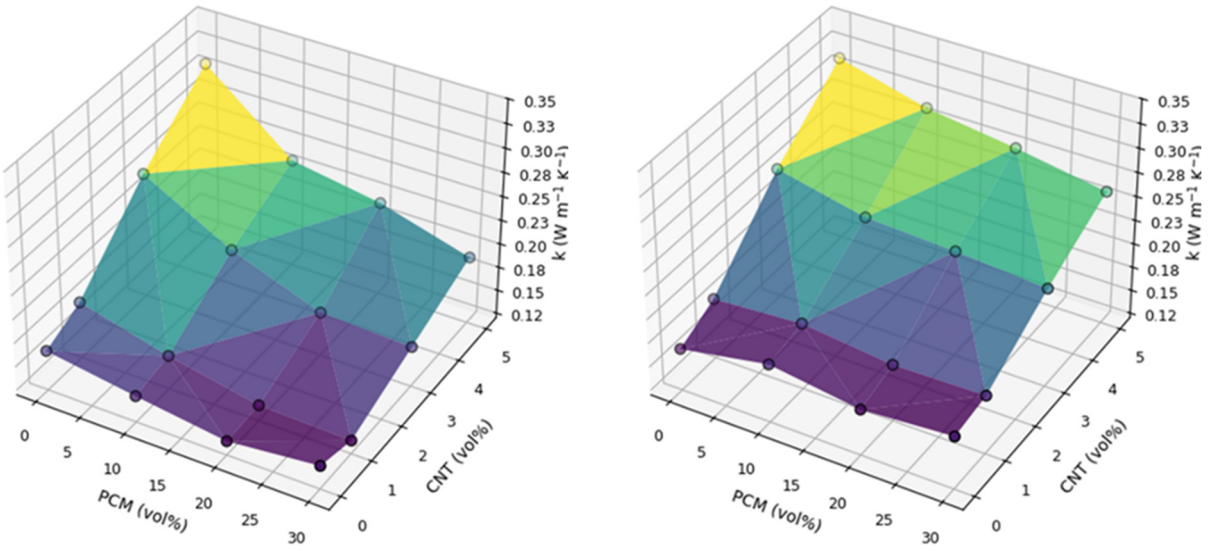

(**a**) (**b**)

Figure 9. Thermal conductivity of TPU/MWCNT/PCM composites as a function of CNT and PCM content at (**a**) 20 °C and (**b**) 40 °C.

Table 6. Thermal conductivity values (in W m^{-1} K^{-1}) of neat TPU and the prepared nanocomposites as a function of the temperature.

Sample	5 °C	10 °C	15 °C	20 °C	25 °C	30 °C	35 °C	40 °C	45 °C	50 °C
TPU	0.160	0.161	0.163	0.162	0.161	0.162	0.162	0.164	0.165	0.166
TPU_10M28D	0.174	0.169	0.162	0.148	0.155	0.174	0.179	0.181	0.183	0.18
TPU_20 M28D	0.173	0.163	0.158	0.135	0.135	0.162	0.166	0.168	0.170	0.170
TPU_30 M28D	0.193	0.181	0.165	0.145	0.128	0.168	0.174	0.175	0.177	0.177
TPU_1MWCNT	0.179	0.179	0.180	0.180	0.181	0.182	0.183	0.183	0.183	0.183
TPU_1MWCNT_10M28D	0.189	0.185	0.177	0.155	0.155	0.186	0.188	0.190	0.190	0.191
TPU_1MWCNT_20M28D	0.184	0.175	0.162	0.137	0.151	0.175	0.179	0.180	0.180	0.181
TPU_1MWCNT_30M28D	0.190	0.180	0.161	0.134	0.142	0.175	0.180	0.182	0.182	0.183
TPU_3MWCNT	0.250	0.253	0.254	0.251	0.253	0.254	0.255	0.256	0.257	0.258
TPU_3MWCNT_10M28D	0.240	0.235	0.225	0.201	0.213	0.231	0.235	0.235	0.236	0.236
TPU_3MWCNT_20M28D	0.238	0.228	0.217	0.166	0.193	0.224	0.231	0.231	0.230	0.233
TPU_3MWCNT_30M28D	0.235	0.227	0.209	0.162	0.180	0.217	0.223	0.224	0.225	0.225
TPU_5MWCNT	0.302	0.305	0.307	0.307	0.309	0.311	0.311	0.313	0.313	0.313
TPU_5MWCNT_10M28D	0.285	0.279	0.268	0.233	0.259	0.285	0.290	0.289	0.289	0.292
TPU_5MWCNT_20M28D	0.283	0.273	0.257	0.218	0.229	0.269	0.277	0.276	0.276	0.279
TPU_5MWCNT_30M28D	0.267	0.253	0.232	0.191	0.212	0.252	0.260	0.260	0.261	0.265

Numerical simulation was carried out to model the transient heat transfer through a 1.5 cm thick TPU–PCM composite layer representing a cooling pad applied to a heat source maintained at 50 °C. The opposite surface of the layer was assumed to be thermally insulated, reproducing the condition of a device attached to a warm component and exposed to ambient air. This simplified one-dimensional geometry allows isolating the influence of the composite's thermal properties on the rate and depth of heat penetration. The purpose of the simulation was to evaluate how changes in matrix thermal conductivity, such as those induced by MWCNT addition, affect the temperature distribution, melting dynamics of the PCM, and overall efficiency of thermal energy storage during heating. The study aimed to assess how increasing the matrix thermal conductivity, for instance through MWCNT addition, affects the temperature field evolution and the efficiency of PCM activation. In this framework, two representative formulations were selected for

modeling: TPU_30M28D and TPU_5MWCNT_30M28D. TPU_30M28D corresponds to the composite with the highest PCM content and no MWCNTs, representing the reference material with the lowest thermal conductivity. TPU_5MWCNT_30M28D, on the other hand, has the same PCM content but the maximum amount of MWCNTs, thus exhibiting the highest thermal conductivity among the tested compositions. This provides a meaningful comparison between a baseline thermally insulating composite and an enhanced thermally conductive one. In such systems, the PCM acts as a thermal buffer, storing heat as latent energy during melting and releasing it upon solidification. However, the efficiency of this mechanism strongly depends on how quickly heat can propagate from the hot interface to the PCM microcapsules dispersed within the TPU matrix. In materials with low thermal conductivity, the heat front advances slowly, and only a thin superficial layer of PCM undergoes the phase change in a given time. As a result, most of the latent capacity remains unexploited. Increasing λ (for instance by adding conductive fillers such as MWCNTs) enhances the thermal diffusivity of the composite, allowing the temperature gradient to penetrate more rapidly and activating a larger PCM fraction within the same time interval. This balance between fast activation and long-term heat buffering is crucial for optimizing thermal management materials.

Figure 10a,b show the space–time maps of temperature for TPU_30M28D and TPU_30M28D_5MWCNT samples, respectively. The color scale indicates the local temperature evolution as a function of both position and time, providing a clear visualization of the heating front propagation inside the samples. In both cases, the heat penetrates progressively from the left boundary (in contact with the hot surface) toward the opposite adiabatic side. At early times ($t < 50$ s), the temperature rise is confined to a few millimeters near the surface, while the inner region remains close to the initial temperature. As heating continues, the thermal front gradually advances, and the region undergoing phase transition (around the paraffin melting temperature, $T_m \approx 28$ °C) expands deeper into the material. A direct comparison between Figure 10a,b highlights the strong influence of thermal conductivity on the heat diffusion rate. In TPU_5MWCNT_30M28D, which contains MWCNTs and therefore has higher λ(T), the temperature gradients are smoother and the 28 °C isotherm (corresponding to the onset of melting) propagates significantly faster through the thickness. On the other hand, TPU_30M28D, characterized by a lower thermal conductivity, the heating front advances more slowly, and a larger portion of the sample remains below the melting temperature for most of the simulation time. This behavior is quantitatively confirmed by the evolution of the average liquid fraction of the PCM, shown in Figure 11. The curve represents the time evolution of the PCM melting process, expressed as the spatially averaged liquid fraction across the sample thickness. At early time ($t < 50$ s), both samples show a similar and slow initial increase, corresponding to surface PCM melting. As time progresses, TPU_5MWCNT_30M28D displays a noticeably faster rise in liquid fraction compared to TPU_30M28D. After 1000 s of exposure to the 50 °C surface, the fraction of molten PCM reaches approximately 0.68 for TPU_5MWCNT_30M28D, whereas TPU_30M28D reaches only 0.50. These results clearly indicate that enhancing the thermal conductivity of the samples substantially accelerates the activation of the PCM. A higher λ value allows heat to penetrate deeper into the material, enabling a larger PCM volume to participate in the phase transition within the same time frame. From a functional perspective, this leads to a faster release of latent heat capacity, which is advantageous for rapid thermal regulation or short-term heat absorption applications. However, increasing thermal conductivity also accelerates temperature equalization within the material, which may shorten the duration of the cooling effect and reduce the composite's ability to attenuate temperature peaks over extended periods [58,59].

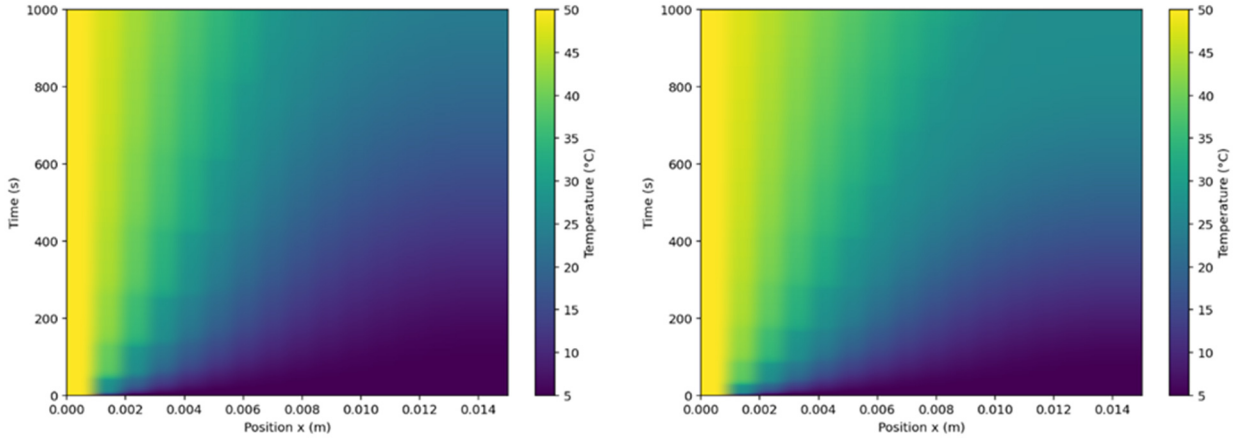

Figure 10. Space–time temperature maps obtained from the 1D transient heat conduction model for a 1.5 cm TPU/PCM slab initially at 5 °C and exposed to a 50 °C boundary: (**a**) TPU_30M28D and (**b**) TPU_5MWCNT _30M28D.

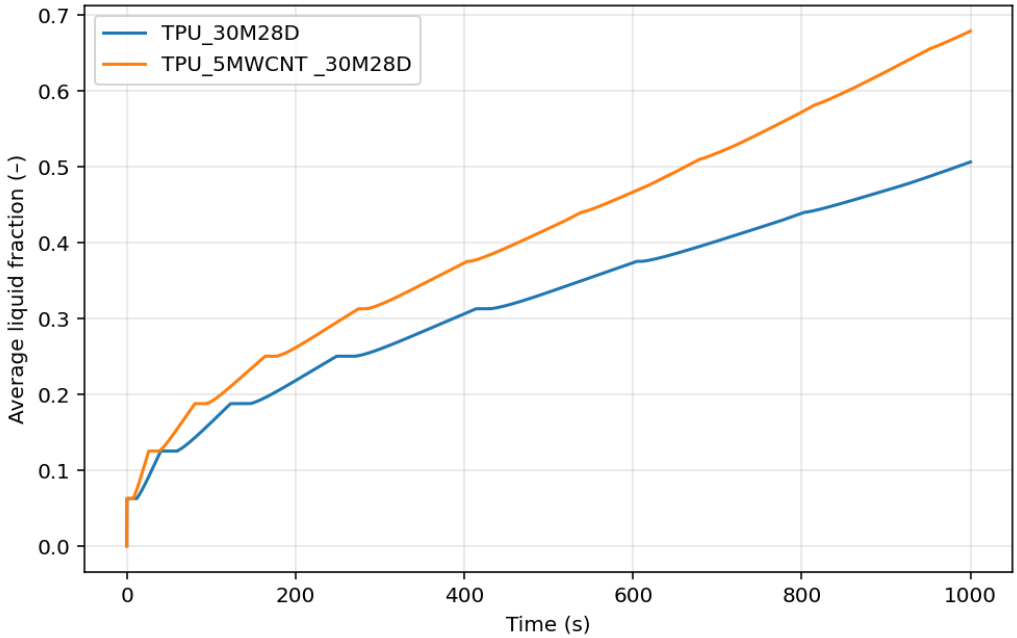

Figure 11. Evolution of the average liquid fraction of PCM during heating from 5 °C to 50 °C for TPU_30M28D and TPU_5MWCNT _30M28D samples.

4. Conclusions

This study demonstrated that the combined incorporation of multi-walled carbon nanotubes and microencapsulated paraffin-based phase change materials into thermoplastic polyurethane enables the design of composites with tunable thermal transport and latent heat storage properties. The inclusion of PCM microcapsules systematically reduced the thermal conductivity at 25 °C from 0.162 $W \cdot m^{-1} \cdot K^{-1}$ for neat TPU to 0.145 $W \cdot m^{-1} \cdot K^{-1}$ at 30 vol.% PCM, reflecting the insulating character of paraffin. Conversely, MWCNTs markedly enhanced heat transfer, increasing the conductivity up to 0.31 $W \cdot m^{-1} \cdot K^{-1}$ at 5 vol.% MWCNTs, corresponding to an improvement of nearly 90% compared to neat TPU. The interplay between these two fillers demonstrated a synergistic effect; MWCNT networks compensated for the reduced conductivity induced by PCMs while preserving their latent heat functionality. Temperature-dependent diffusivity and conductivity measurements revealed distinct non-linear behavior around 25 °C, associated with the paraffin

melting transition. During this phase change, part of the thermal energy was absorbed as latent heat, causing a transient decrease in apparent diffusivity. Numerical simulations of one-dimensional transient heating performed on TPU_30M28D and TPU_30M28D_5MWCNT samples showed that increasing thermal conductivity via 5 vol.% MWCNTs addition markedly accelerated heat penetration and PCM activation. After 1000 s, the average liquid fraction increased from ≈ 50% to ≈ 68% with MWCNTs, and the time to reach 50% of PCM activation decreased from ≈ 1000 s to ≈ 450 s. This demonstrated that CNT-enhanced matrices promoted faster PCM activation and more efficient utilization of the stored latent heat during cyclic thermal loading. Considering the application niche (high-performance wearable thermal patches), the conductivity gain offered by carbon nanotube networks compensates for filler cost, offering a commensurate energy-buffering dynamic benefit. However, alternative conductive nanofillers may also be considered for cost reduction in broader-scale deployment. Overall, these results highlighted the ability of the TPU/MWCNT/PCM system to combine rapid heat dissipation with dynamic thermal buffering, providing valuable design guidelines for multifunctional materials in flexible electronics, energy storage devices, thermal management of batteries, and smart building technologies. The combination of experimental characterization and numerical modeling offered a quantitative framework for optimizing both steady-state and transient thermal behavior in polymer-based energy management systems.

Author Contributions: Conceptualization, A.D., A.P. and D.R.; methodology, D.R.; software, D.R.; validation, D.R.; formal analysis, D.R.; investigation, D.R.; resources, D.R.; data curation, D.R.; writing—original draft preparation, D.R.; writing—review and editing, A.D. and D.R.; visualization, D.R.; supervision, A.P. All authors have read and agreed to the published version of the manuscript.

Funding: This research was partially funded by the Department of Excellence 2023–2027 (DE 23–27) pro-gram, financed by the Italian Ministery of University (MUR).

Data Availability Statement: The raw data supporting the conclusions of this article will be made available by the authors on request.

Conflicts of Interest: The authors declare no conflicts of interest.

References

1. Lv, Y.-G.; Zhang, G.-P.; Wang, Q.-W.; Chu, W.-X. Thermal Management Technologies Used for High Heat Flux Automobiles and Aircraft: A Review. *Energies* **2022**, *15*, 8316. [CrossRef]
2. Mao, S.; Liu, Y.; Wu, X.; Zhang, L.; Chen, J.; Zhou, T. Thermal energy storage performance, application and challenge of phase change materials: A review. *Energy Storage Sav.* **2025**, *4*, 300–322. [CrossRef]
3. Alawadhi, E.M.; Amon, C.H. PCM thermal control unit for portable electronic devices: Experimental and numerical studies. *IEEE Trans. Compon. Packag. Technol.* **2003**, *26*, 116–125. [CrossRef]
4. Zhai, X.; Xu, Z.; Zhang, W.; Zhang, Q.; Yang, X.; Qu, J.; Liu, G.; Yu, B. Phase change thermal energy storage: Materials and heat transfer enhancement methods. *J. Energy Storage* **2025**, *123*, 116778. [CrossRef]
5. Tyagi, V.V.; Buddhi, D. PCM thermal storage in buildings: A state of art. *Renew. Sustain. Energy Rev.* **2007**, *11*, 1146–1166. [CrossRef]
6. Mondal, S. Phase change materials for smart textiles—An overview. *Appl. Therm. Eng.* **2008**, *28*, 1536–1550. [CrossRef]
7. Zalba, B.; Marín, J.M.; Cabeza, L.F.; Mehling, H. Review on thermal energy storage with phase change: Materials, heat transfer analysis and applications. *Appl. Therm. Eng.* **2003**, *23*, 251–283. [CrossRef]
8. Fredi, G.; Dorigato, A.; Fambri, L.; Pegoretti, A. Multifunctional structural composites for thermal energy storage. *Multifunct. Mater.* **2020**, *3*, 042001. [CrossRef]
9. Galvagnini, F.; Dorigato, A.; Fambri, L.; Pegoretti, A. Development of Novel Polypropylene Syntactic Foams Containing Paraffin Microcapsules for Thermal Energy Storage Applications. *Molecules* **2022**, *27*, 8520. [CrossRef]
10. Valentini, F.; Dorigato, A.; Fambri, L.; Pegoretti, A. Novel EPDM/Paraffin Foams for Thermal Energy Storage Applications. *Rubber Chem. Technol.* **2021**, *94*, 432–448. [CrossRef]

11. Wang, S.; Du, R.; Li, T. Progress and perspective on thermal conductivity enhancement of phase change materials. *Sci. Bull.* **2024**, *69*, 3176–3179. [CrossRef] [PubMed]
12. Shchukina, E.M.; Graham, M.; Zheng, Z.; Shchukin, D.G. Nanoencapsulation of phase change materials for advanced thermal energy storage systems. *Chem. Soc. Rev.* **2018**, *47*, 4156–4175. [CrossRef] [PubMed]
13. Fredi, G.; Dorigato, A.; Fambri, L.; Unterberger, S.H.; Pegoretti, A. Effect of phase change microcapsules on the thermo-mechanical, fracture and heat storage properties of unidirectional carbon/epoxy laminates. *Polym. Test.* **2020**, *91*, 106747. [CrossRef]
14. Liao, H.; Guo, S.; Liu, Y.; Wang, Q. Form-stable phase change composites with high thermal conductivity and adjustable thermal management capacity. *Sol. Energy Mater. Sol. Cells* **2021**, *221*, 110881. [CrossRef]
15. Pielichowska, K.; Pielichowski, K. Phase change materials for thermal energy storage. *Prog. Mater. Sci.* **2014**, *65*, 67–123. [CrossRef]
16. Dorigato, A.; Rigotti, D.; Pegoretti, A. Thermoplastic Polyurethane Blends with Thermal Energy Storage/Release Capability. *Front. Mater.* **2018**, *5*, 58. [CrossRef]
17. Rigotti, D.; Dorigato, A.; Pegoretti, A. 3D printable thermoplastic polyurethane blends with thermal energy storage/release capabilities. *Mater. Today Commun.* **2018**, *15*, 228–235. [CrossRef]
18. Rigotti, D.; Dorigato, A.; Pegoretti, A. Low-cycle fatigue behavior of flexible3Dprinted thermoplastic polyurethane blends for thermal energy storage/release applications. *J. Appl. Polym. Sci.* **2020**, *138*, 49704. [CrossRef]
19. Yang, W.; Li, X.; Li, C.; Deng, J.; Du, Y.; Zhang, G. High Antileakage and Thermal Conductivity Composite Phase-Change Material with Anisotropy Expanded Graphite for Battery Thermal Management. *ACS Appl. Energy Mater.* **2023**, *6*, 9698–9708. [CrossRef]
20. Han, Z.; Fina, A. Thermal conductivity of carbon nanotubes and their polymer nanocomposites: A review. *Prog. Polym. Sci.* **2011**, *36*, 914–944. [CrossRef]
21. Huang, C.; Qian, X.; Yang, R. Thermal conductivity of polymers and polymer nanocomposites. *Mater. Sci. Eng. R Rep.* **2018**, *132*, 1–22. [CrossRef]
22. Kim, P.; Shi, L.; Majumdar, A.; McEuen, P.L. Thermal transport measurements of individual multiwalled nanotubes. *Phys. Rev. Lett.* **2001**, *87*, 215502. [CrossRef]
23. Fenta, E.W.; Mebratie, B. Advancements in Carbon Nanotube-Polymer Composites: Enhancing Properties and Applications through Advanced Manufacturing Techniques. *Heliyon* **2024**, *10*, 03012. [CrossRef]
24. Zeinedini, A.; Akhavan-Safar, A.; da Silva, L.F.M. The role of agglomeration in the physical properties of CNTs/polymer nanocomposites: A literature review. *Proc. Inst. Mech. Eng. Part L J. Mater. Des. Appl.* **2025**.
25. Iqbal, K.; Khan, A.; Sun, D.; Ashraf, M.; Rehman, A.; Safdar, F.; Basit, A.; Maqsood, H.S. Phase change materials, their synthesis and application in textiles—A review. *J. Text. Inst.* **2019**, *110*, 625–638. [CrossRef]
26. Mokhtari Yazdi, M.; Sheikhzadeh, M.; Borhani, S. Modeling the heat transfer in a PCM cooling vest. *J. Text. Inst.* **2014**, *106*, 1003–1012. [CrossRef]
27. Cui, G.; Wang, C. Applications and development trends of textile materials in sports: A review. *Alex. Eng. J.* **2025**, *126*, 491–506. [CrossRef]
28. Rigotti, D.; Dorigato, A.; Pegoretti, A. Multifunctional 3D-Printed Thermoplastic Polyurethane (TPU)/Multiwalled Carbon Nanotube (MWCNT) Nanocomposites for Thermal Management Applications. *Appl. Sci.* **2024**, *14*, 9614. [CrossRef]
29. Mikhaylov, A.A.; Sladkevich, S.; Medvedev, A.G.; Prikhodchenko, P.V.; Gun, J.; Sakharov, K.A.; Xu, Z.J.; Kulish, V.; Nikolaev, V.A.; Lev, O. Enhanced Thermal Buffering of Phase Change Materials by the Intramicrocapsule Sub per Mille CNT Dopant. *ACS Appl. Mater. Interfaces* **2020**, *12*, 16227–16235. [CrossRef]
30. Hu, J.; Huang, W.; Ge, X.; Wang, C.; Zhang, G.; Chen, Y.; Tu, C. Preparation of flexible composite phase change material with high thermal conductivity for battery thermal management. *J. Energy Storage* **2024**, *100*, 113485. [CrossRef]
31. *ASTM E2716*; Standard Test Method for Determining Specific Heat Capacity by Sinusoidal Modulated Temperature Differential Scanning Calorimetry. ASTM: West Conshohocken, PA, USA, 2023.
32. Günther, D.; Steimle, F. Mixing rules for the specific heat capacities of several HFC-mixtures. *Int. J. Refrig.* **1997**, *20*, 235–243. [CrossRef]
33. Voller, V.R.; Cross, M.; Markatos, N.C. An enthalpy method for convection/diffusion phase change. *Int. J. Numer. Methods Eng.* **1987**, *24*, 271–284. [CrossRef]
34. Fredi, G.; Ronconi, G.; Galvagnini, F.; Mazzanti, V.; Zanelli, M.; Mollica, F.; Dorigato, A. Modeling the thermal behavior of multifunctional syntactic foams containing phase change materials for heat management applications. *Polym. Compos.* **2024**, *45*, 15590–15603. [CrossRef]
35. Mahgerefteh, H.; Rykov, Y.; Denton, G. Courant, Friedrichs and Lewy (CFL) impact on numerical convergence of highly transient flows. *Chem. Eng. Sci.* **2009**, *64*, 4969–4975. [CrossRef]
36. Lashgari, S.; Arabi, H.; Mahdavian, A.R.; Ambrogi, V. Thermal and morphological studies on novel PCM microcapsules containing n-hexadecane as the core in a flexible shell. *Appl. Energy* **2017**, *190*, 612–622. [CrossRef]
37. Pötschke, P.; Fornes, T.D.; Paul, D.R. Rheological behavior of multiwalled carbon nanotube/polycarbonate composites. *Polymer* **2002**, *43*, 3247–3255. [CrossRef]

38. Arrigo, R.; Malucelli, G. Rheological Behavior of Polymer/Carbon Nanotube Composites: An Overview. *Materials* **2020**, *13*, 2771. [CrossRef] [PubMed]
39. Lee, C.-F.; Chen, C.-W.; Rwei, S.-P.; Chuang, F.-S. Thermal Behavior and Morphology of Thermoplastic Polyurethane Derived from Different Chain Extenders of 1,3- and 1,4-Butanediol. *Appl. Sci.* **2021**, *11*, 698. [CrossRef]
40. Puszka, A.; Kultys, A. New thermoplastic polyurethane elastomers based on aliphatic diisocyanate. *J. Therm. Anal. Calorim.* **2017**, *128*, 407–416. [CrossRef]
41. Wang, P.-S.; Chiu, W.-Y.; Chen, L.-W.; Denq, B.-L.; Don, T.-M.; Chiu, Y.-S. Thermal degradation behavior and flammability of polyurethanes blended with poly(bispropoxyphosphazene). *Polym. Degrad. Stab.* **1999**, *66*, 307–315. [CrossRef]
42. Herrera, M.; Matuschek, G.; Kettrup, A. Thermal degradation of thermoplastic polyurethane elastomers (TPU) based on MDI. *Polym. Degrad. Stab.* **2002**, *78*, 323–331. [CrossRef]
43. Wang, C.; Chen, X.; Xie, H.; Cheng, R. Effects of carbon nanotube diameter and functionality on the properties of soy polyol-based polyurethane. *Compos. Part A Appl. Sci. Manuf.* **2011**, *42*, 1620–1626. [CrossRef]
44. Ciecierska, E.; Jurczyk-Kowalska, M.; Bazarnik, P.; Kowalski, M.; Krauze, S.; Lewandowska, M. The influence of carbon fillers on the thermal properties of polyurethane foam. *J. Therm. Anal. Calorim.* **2016**, *123*, 283–291. [CrossRef]
45. Su, S.P.; Xu, Y.H.; China, P.R.; Wilkie, C.A. 16—Thermal degradation of polymer–carbon nanotube composites. In *Polymer–Carbon Nanotube Composites*; McNally, T., Pötschke, P., Eds.; Woodhead Publishing: Cambridge, UK, 2011; pp. 482–510.
46. He, Y.-L.; Xie, T. Advances of thermal conductivity models of nanoscale silica aerogel insulation material. *Appl. Therm. Eng.* **2015**, *81*, 28–50. [CrossRef]
47. Dashora, P.; Gupta, G. On the temperature dependence of the thermal conductivity of linear amorphous polymers. *Polymer* **1996**, *37*, 231–234. [CrossRef]
48. Ivan, K.; Pavol, K.; Jan, V.; Marta, H.; Zora, J. Temperature dependence of thermal properties of thermoplastic polyurethane-based carbon nanocomposites. *AIP Conf. Proc.* **2016**, *1768*, 020019. [CrossRef]
49. Abohamzeh, E.; Sheikholeslami, M. Thermal Properties of Carbon Nanotube. In *Handbook of Carbon Nanotubes*; Abraham, J., Thomas, S., Kalarikkal, N., Eds.; Springer International Publishing: Cham, Switzerland, 2022; pp. 149–172.
50. Cao, J.; Yan, X.H.; Xiao, Y. Specific heat of Single-Walled Carbon Nanotubes: A Lattice Dynamics Study. *J. Phys. Soc. Jpn.* **2003**, *72*, 2256–2259. [CrossRef]
51. Huang, X.; Wang, J.; Eres, G.; Wang, X. Thermophysical properties of multi-wall carbon nanotube bundles at elevated temperatures up to 830K. *Carbon* **2011**, *49*, 1680–1691. [CrossRef]
52. Pradhan, N.R.; Duan, H.; Liang, J.; Iannacchione, G.S. The specific heat and effective thermal conductivity of composites containing single-wall and multi-wall carbon nanotubes. *Nanotechnology* **2009**, *20*, 245705. [CrossRef]
53. Zhan, H.; Chen, Y.W.; Shi, Q.Q.; Zhang, Y.; Mo, R.W.; Wang, J.N. Highly aligned and densified carbon nanotube films with superior thermal conductivity and mechanical strength. *Carbon* **2022**, *186*, 205–214. [CrossRef]
54. Fatahi, H.; Claverie, J.; Poncet, S. Thermal Characterization of Phase Change Materials by Differential Scanning Calorimetry: A Review. *Appl. Sci.* **2022**, *12*, 12019. [CrossRef]
55. Sun, X.; Lee, K.O.; Medina, M.A.; Chu, Y.; Li, C. Melting temperature and enthalpy variations of phase change materials (PCMs): A differential scanning calorimetry (DSC) analysis. *Phase Transit.* **2018**, *91*, 667–680. [CrossRef]
56. *ISO 11357-3*; Plastics—Differential scanning calorimetry (DSC)—Part 3: Determination of temperature and enthalpy of melting and crystallization. Geneva, Switzerland, 2018.
57. *ASTM E2716-09*; Standard Test Method for Determining Specific Heat Capacity by Modulated Differential Scanning Calorimetry. ASTM: West Conshohocken, PA, USA, 2015.
58. Khodadadi, J.M.; Hosseinizadeh, S.F. Nanoparticle-enhanced phase change materials (NEPCM) with great potential for improved thermal energy storage. *Int. Commun. Heat Mass Transf.* **2007**, *34*, 534–543. [CrossRef]
59. Fan, L.; Khodadadi, J.M. Thermal conductivity enhancement of phase change materials for thermal energy storage: A review. *Renew. Sustain. Energy Rev.* **2011**, *15*, 24–46. [CrossRef]